Distributed Extension across the Ethiopian Rift and Plateau Illuminated by Joint Inversion of Surface Waves and Scattered Body Waves

J. Petruska[1], Z. Eilon [1]

[1]University of California, Santa Barbara

Contents of this file

1. Table T1
2. Text S1 to S5
3. Figures S1 to S12

Additional Supporting Information (Files uploaded separately)

1. Data fit images S12 to S92
2. RF quality control images S93 - S120

Introduction Below we present several figures to support observations and conclusions we develop in the main document. All data are developed from the same two data sets presented in the main document, and figures presented show interim steps that may clarify decisions made during interpretation. Figure S1 shows the raw H-κ derived Moho and Vp/Vs results. Figures S2 - S7 seek to show inherent difficulty and error in forward

---

Corresponding author: J. Petruska, , Department of Earth Science, University of California, Santa Barbara, 1006 Webb Hall, Santa Barbara, CA, 93106, USA. (jonpetruska@ucsb.edu)

modelling geotherms into shear velocities. S8 - S10 display results used for interpretation, that were not included in the main document due to size constraints. Figure S11 displays a test modified from the methodology of Ogden, Bastow, Gilligan, and Rondenay (2019), comparing the results of H-κ stacking before and after quality controls. Zipped files contain results seen in S8 - S10, and S11 for each station inverted for shear velocity.

Receiver Function Derived Crustal Thickness and Vp/Vs Ratios S1. Crustal thickness and Vp/Vs ratios are taken as the maximum of the normalized H-κ surface at each station. A Vp of 6.3 is used, and phase weights of 0.7, 0.2, 0.1 are used in the H-κ stacking process. Crustal thickness results are similar to those of the inverted results, and trends discussed in the inverted crustal thickness section are relevant here as well. Our Vp/Vs ratios are similar to those of (Hammond et al., 2011) in the western Ethiopian Plateau (1.7 - 1.9). There is broader uncertainty with the Vp/Vs ratio than the crustal thickness, even for well constrained H-κ stack surfaces, as can be seen below in the inversion data fit subsection.

Geotherm Gridsearch Considerations S2.

It is difficult to forward model shear velocities from a continental geotherm that can closely predict shear velocities using existing scaling relationships (Dalton & Faul, 2010). Cammarano, Goes, Deuss, and Giardini (2005); Cammarano and Romanowicz (2007) discuss the difficulties in matching velocity models from geophysical observations and compositional, thermal, and anisotropic effects in the Earth. Calculating a shear velocity profile from geotherms cannot, as far as we currently understand it, perfectly predict shear velocity structures. Using different forward modeling methods, with the same input geotherm, can produce shear velocities at the same depth as different as $\sim$0.4 km/s. To

calculate shear velocities, we use calculations from (Takei, 2017; Jackson & Faul, 2010; Faul & Jackson, 2005; Priestley & McKenzie, 2013) and an anharmonic calculation to show variance between these methods.

Deviation between observed and modeled Vs are most apparent between 30 and 60 km, where the geotherms change slope to an adiabatic gradient. Determining how to better forward model shear velocities from a geotherm is beyond the scope of this research, so we instead use a geotherm gridsearch, minimizing misfit between predicted and observed Vs between 60 and 120 km, the depths our phase velocity data are most sensitive.

Geotherm Parameter Gridsearch S3. Because of the inherent difficulty in perfectly matching shear velocity observations forward modeled from a geotherm, we gridsearch crustal thickness, mantle potential temperature (T_m), surface heat flow (Q_0), and radiogenic heat production (A_0). This determines a range of parameters that produce well-fit shear velocity models by minimizing the misfit between the forward modeled geotherm and the observed shear velocity of each group. Because of the notable spread in shear velocity estimates seen above, we chose to use a single method during gridsearching, Takei (2017), as this method generally provided better fits to the observed shear velocities. Note that we do not show the results of crustal thickness, as we found our geotherms insensitive to it.

Inversion Data Fit and H-κ stacks S4. For each station we jointly inverted, we have included three images similar to figure 4 in the manuscript. The naming scheme is as follows, where STATION NAME refers to the inverted station. STATION NAME_data_pred.jpg : The fit of the mean surface wave, receiver function, and H-κ model. STATION NAME_HK_fit.jpg : The same as the previous image, but with ev-

ery H-κ solution from shear velocity models plotted in the gridsearch area. STATION NAME_vs_prof.jpg : The inverted shear velocity profile. The red line indicates the mean model, the grey patch is the 1σ, and white patch bounded in light grey is the 2σ. The posterior distribution of Moho solutions is plotted as a red histogram, and the best fit Moho depth and standard deviation are denoted by the horizontal dashed black line. An example of the three images is shown below for clarification.

H-κ Reliability Test S5. Ogden et al. (2019) found that many H-κ derived estimates were unreliable within the EPL. Using an automatic method to perturb input parameters for H-κ stacking, they found that stations within flood basalts produced unreliable H-κ stacks with high standard deviation, low SNR, and broad low amplitude arrival phases. Such H-κ stacks failed to resolve a high energy maximum for the Moho and κ due to a gradational Moho, complex crust, or sediments and basalts.

To test the reliability our H-κ stack results, we modified Ogden et al. (2019)'s random input perturbation procedure on several stations in the region using receiver functions from before the DBSCAN process (raw) and those that passed the DBSCA process (cleaned). We randomly perturbed the Vp from [6.2: 0.1: 6.8], the maximum filter frequency from [0.1: 0.1: 2.0] Hz before calculating the receiver function, the weight of the Ps phase from [0.4: 0.05: 0.9], the $PpPs$ phase from [0.1: 0.05: 0.6], and the $PpSs + PsPs$ phase from [0.0: 0.05: 0.5] (with total phase weights required to sum to 1.0). These random perturbations were run 5000 times for the raw and cleaned receiver functions. A robust result was expected to display a distinct high energy maximum in the H-κ surface, closely clustered mean model solutions between different input parameters, a similar mean and mode H-κ for all 5000 models, and an H and κ that were not capped at the edges of the

grid search surface. An example of this process is shown in fig. S11. Raw H-κ stack surfaces (fig. S11a) generally fail to find a high energy maximum - the summation of all H-κ surfaces finds five high energy maxima in which input parameter variability solved to different maxima despite using the same data. The mean H-κ value of the 5000 iterations (40.81, 1.81) is dissimilar to the absolute maximum of the surface (39.9, 1.6). The surface maximum is also capped by the bounds of the κ values. Contrarily, the cleaned H-κ stack surface (fig. S11b) finds a well defined maximum in the H-κ stack surface (37.4, 1.68), which is similar to the mean (37.52, 1.67) of the 5000 best fit H-κ iterations. We note that the difference between raw and cleaned H-κ stack surfaces are not consistently different across all stations, but quality controls still improved the H-κ energy surface. **T1. Moho Depth Table**

Station	**Moho (km)**	**Std (km)**	**Lat**	**Lon**
ABMD	29.25	1.52	11.832	35.583
AMME	37.80	1.41	8.303	39.093
ARBA	28.06	1.76	6.067	37.556
ASOS	33.06	2.10	10.091	34.564
BAHI	35.30	1.70	11.574	37.393
CHEF	31.29	1.44	6.161	38.210
CHGE	34.04	2.86	10.961	36.518
DAQU	32.79	1.24	13.145	37.898
DEBR	27.98	1.52	10.635	35.662
DLMN	36.86	3.22	6.424	39.856
GIDA	34.02	2.42	8.980	34.610
GORE	34.34	1.87	8.150	35.533
GUBA	28.52	1.32	11.271	35.289
GUBL	32.58	1.20	11.179	36.005
HARO	32.00	1.28	9.847	36.310
HDBU	34.55	0.84	9.376	35.651
JAWI	31.48	1.28	11.571	36.491
JIMA	30.88	3.65	7.684	36.831
KIRE	37.23	1.63	9.957	36.869
MELA	28.37	1.44	12.396	35.960

continued on next page

MEND	31.81	0.96	9.787	35.111
MERT	36.59	1.71	10.876	38.266
MGNA	28.80	1.77	12.786	36.404
MUKA	31.89	1.02	12.064	36.374
NEKE	31.22	1.03	9.089	36.523
SERE	38.96	1.89	12.513	37.028
SHAW	33.99	2.13	11.930	36.870
SHER	31.28	1.01	10.594	34.786

Table S1: ds12. A list of Moho thicknesses and standard deviation, in km, from post-inversion shear velocity models.

S1. Moho and Vp/Vs ratio

S2. - S4. Forward modeled Vs from Geotherms

S5. Geotherm Gridsearch Misfits for Group 1

S6. Geotherm Gridsearch Misfits for Group 2

S7. Geotherm Gridsearch Misfits for Group 3

S8. Predicted and Observed Data fit

S9. Predicted and Observed Data fit, H-κ Models

S10. Shear Velocity Model and Moho Distribution

S11. H-κ Stack Testing

References

Cammarano, F., Goes, S., Deuss, A., & Giardini, D. (2005). Is a pyrolitic adiabatic mantle compatible with seismic data? *Earth and Planetary Science Letters*, *232*(3-4), 227–243.

Cammarano, F., & Romanowicz, B. (2007). Insights into the nature of the transition

zone from physically constrained inversion of long-period seismic data. *Proceedings of the National Academy of Sciences*, *104*(22), 9139–9144.

Dalton, C. A., & Faul, U. H. (2010). The oceanic and cratonic upper mantle: Clues from joint interpretation of global velocity and attenuation models. *Lithos*, *120*(1-2), 160–172.

Faul, U. H., & Jackson, I. (2005). The seismological signature of temperature and grain size variations in the upper mantle. *Earth and Planetary Science Letters*, *234*(1-2), 119–134.

Hammond, J. O., Kendall, J.-M., Stuart, G., Keir, D., Ebinger, C., Ayele, A., & Belachew, M. (2011). The nature of the crust beneath the afar triple junction: Evidence from receiver functions. *Geochemistry, Geophysics, Geosystems*, *12*(12).

Jackson, I., & Faul, U. H. (2010). Grainsize-sensitive viscoelastic relaxation in olivine: Towards a robust laboratory-based model for seismological application. *Physics of the Earth and Planetary Interiors*, *183*(1-2), 151–163.

Ogden, C., Bastow, I. D., Gilligan, A., & Rondenay, S. (2019). A reappraisal of the h–κ stacking technique: implications for global crustal structure. *Geophysical Journal International*, *219*(3), 1491–1513.

Priestley, K., & McKenzie, D. (2013). The relationship between shear wave velocity, temperature, attenuation and viscosity in the shallow part of the mantle. *Earth and Planetary Science Letters*, *381*, 78–91.

Takei, Y. (2017). Effects of partial melting on seismic velocity and attenuation: A new insight from experiments. *Annual Review of Earth and Planetary Sciences*, *45*, 447–470.

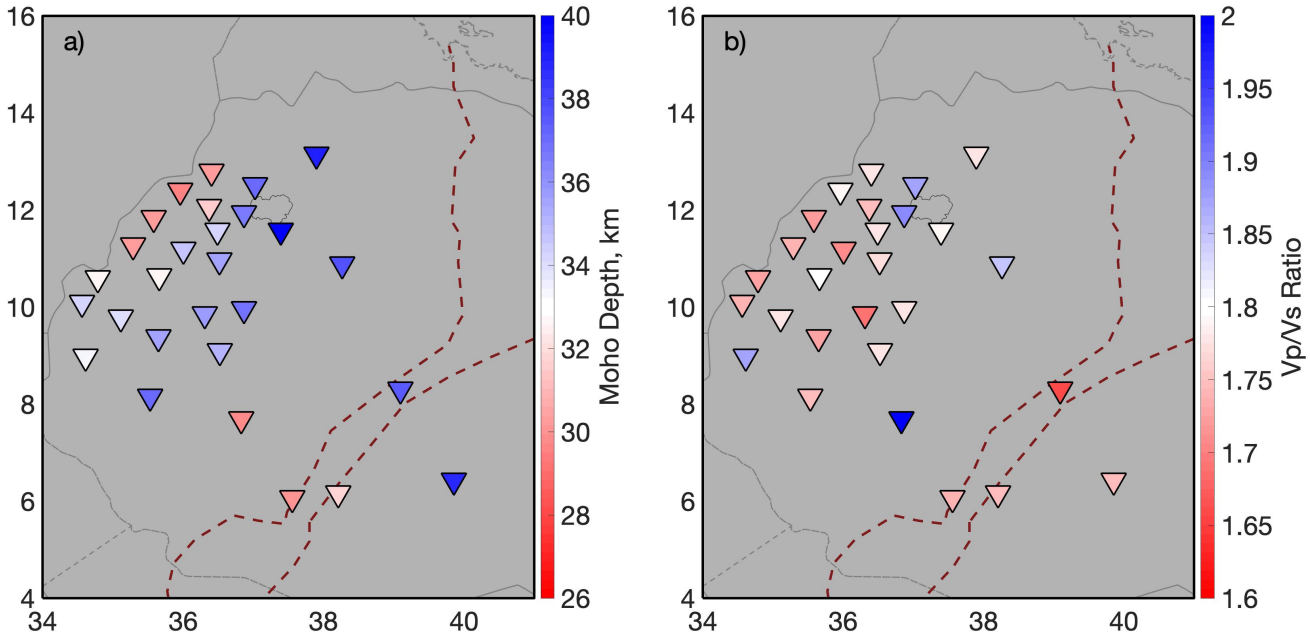

Figure S1. ds01.a) The crustal thicknesses for each station taken as the maximum energy region in the H-κ surface. Warmer colors indicate shallower crust. ds01.b) The Vp/Vs ratio from the same H-κ surface, at each station. Warmer colors indicate a lower Vp/Vs ratio.

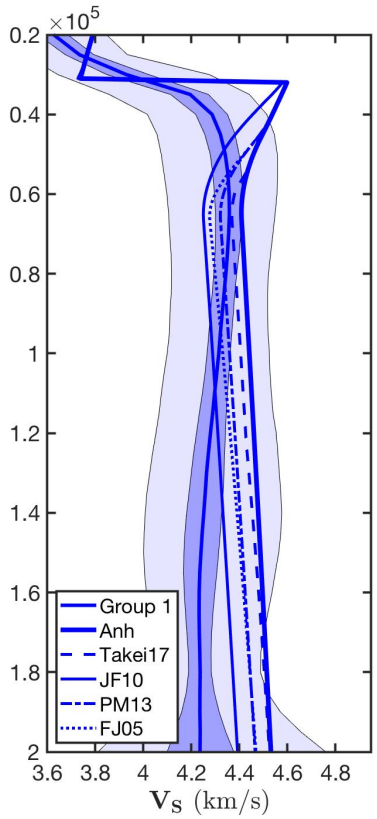

Figure S2. ds02.) The range of modeled Vs by varied methods, of the geotherm best fit to group 1. The group 1 velocity aggregate is plotted in solid dark blue, surrounded by its 1σ (dark blue patch) and 2σ (light blue patch). The anharmonic calculation is also plotted in solid dark blue, but is always faster than the velocity profile. Calculated Vs from (?, ?) are in dashed blue, (Jackson & Faul, 2010) in thin solid blue, (Priestley & McKenzie, 2013) in blue dash-hatches, and (Faul & Jackson, 2005) in blue dots.

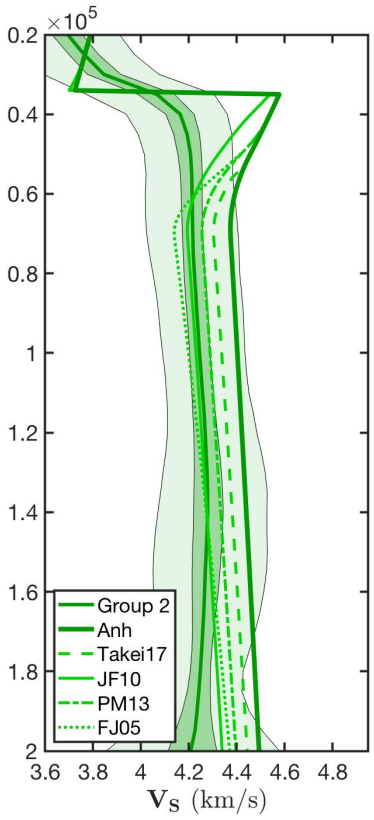

Figure S3. ds03.) The range of modeled Vs by varied methods, of the geotherm best fit to group 2. The group 2 velocity aggregate is plotted in solid dark green, surrounded by its 1σ (dark green patch) and 2σ (light green patch). The anharmonic calculation is also plotted in solid dark green, but is always faster than the velocity profile. Calculated Vs from (?, ?) are in dashed green, (Jackson & Faul, 2010) in thin solid green, (Priestley & McKenzie, 2013) in green dash-hatches, and (Faul & Jackson, 2005) in green dots.

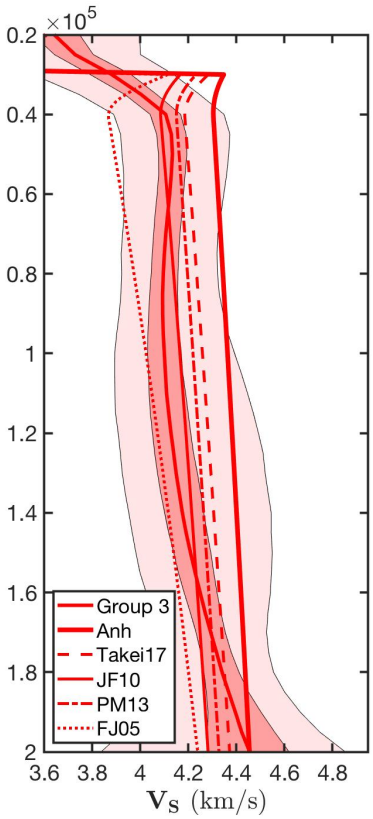

Figure S4. ds04.) The range of modeled Vs by varied methods, of the geotherm best fit to group 3. The group 3 velocity aggregate is plotted in solid dark red, surrounded by its 1σ (dark red patch) and 2σ (light red patch). The anharmonic calculation is also plotted in solid dark red, but is always faster than the velocity profile. Calculated Vs from (?, ?) are in dashed red, (Jackson & Faul, 2010) in thin solid red, (Priestley & McKenzie, 2013) in red dash-hatches, and (Faul & Jackson, 2005) in red dots.

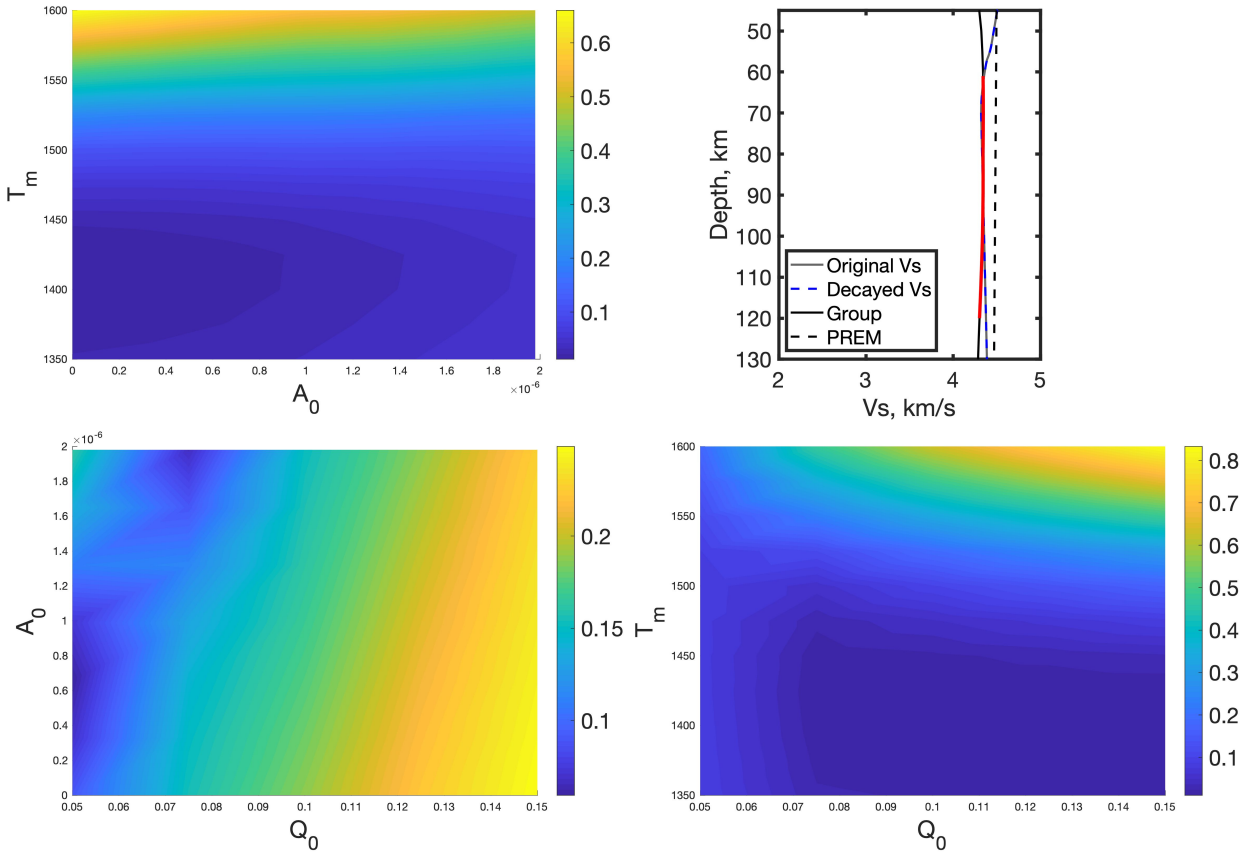

Figure S5. ds05. Misfit surface for Group 1, comparing mantle potential temperatures (T_m), surface heat flow (Q_0) and crustal radiogenic heat production (A_0). Cooler colors indicate lower misfit, warmer colors indicate higher misfit. The shear velocity profile of group 1 (black) is shown in the upper right corner, with the best fit velocity profile before percolation and compaction (grey), and after (dashed blue). PREM is dashed in black, and the depth range used to minimize misfit is highlighted in red on the grou Vs profile.

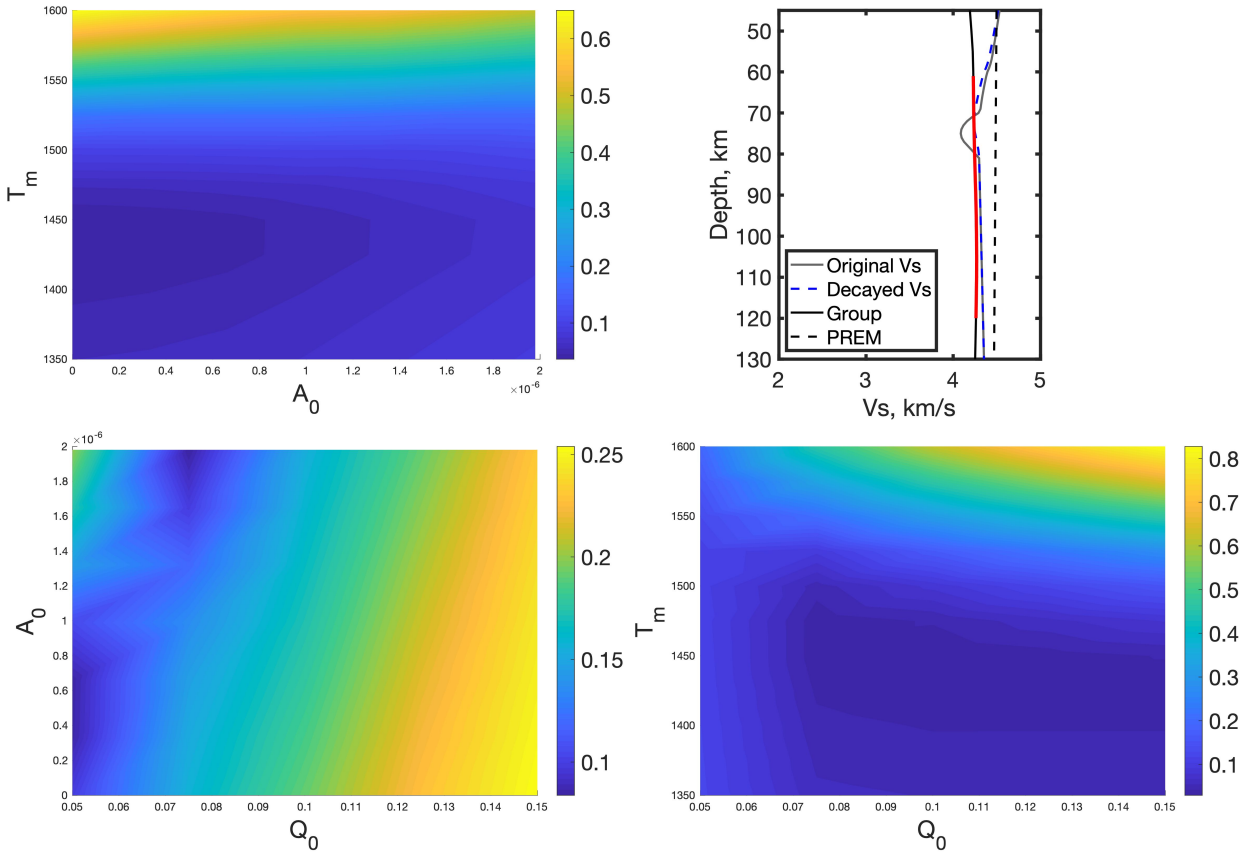

Figure S6. ds06. Misfit surface for Group 2 comparing mantle potential temperatures (T_m), surface heat flow (Q_0) and crustal radiogenic heat production (A_0). Cooler colors indicate lower misfit, warmer colors indicate higher misfit. The shear velocity profile of group 2 (black) is shown in the upper right corner, with the best fit velocity profile before percolation and compaction (grey), and after (dashed blue). PREM is dashed in black, and the depth range used to minimize misfit is highlighted in red on the grou Vs profile.

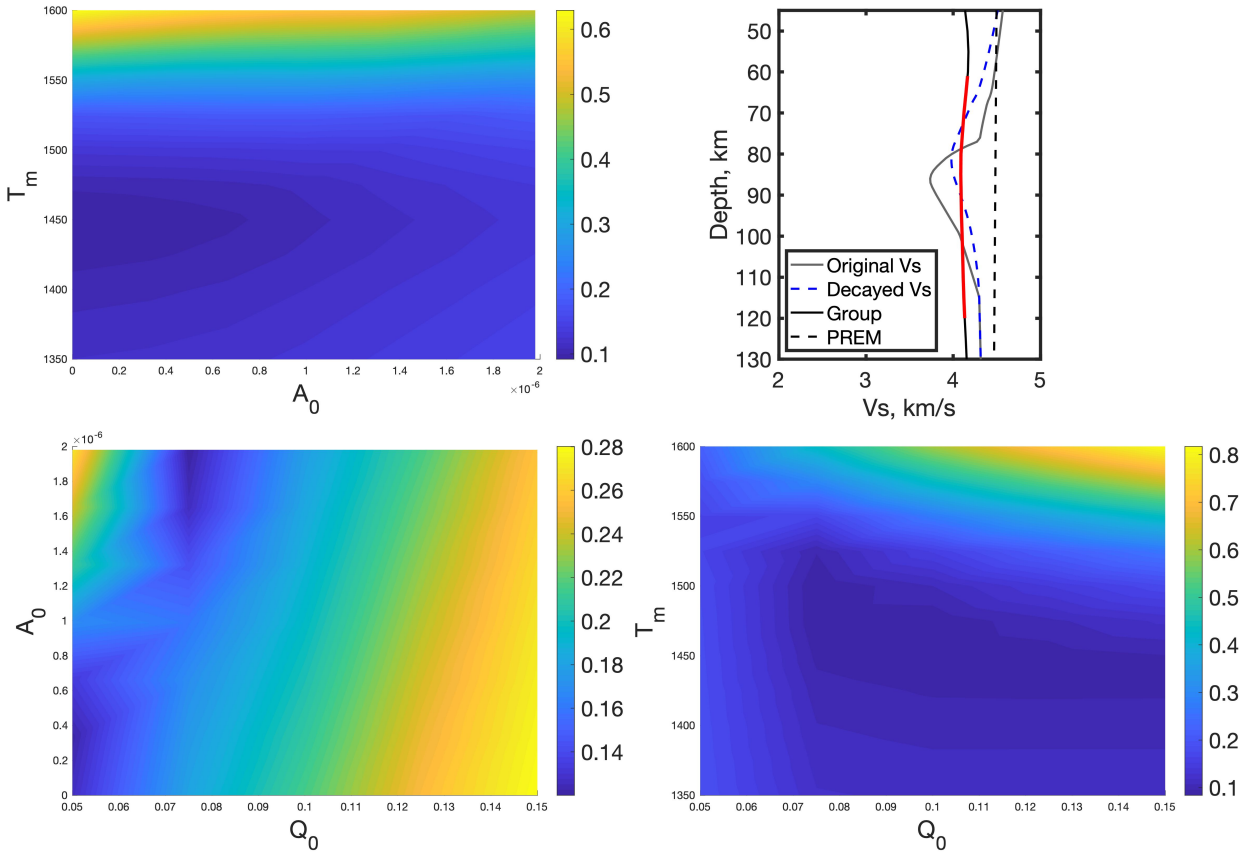

Figure S7. ds07. Misfit surface for Group 3 comparing mantle potential temperatures (T_m), surface heat flow (Q_0) and crustal radiogenic heat production (A_0). Cooler colors indicate lower misfit, warmer colors indicate higher misfit. The shear velocity profile of group 3 (black) is shown in the upper right corner, with the best fit velocity profile before percolation and compaction (grey), and after (dashed blue). PREM is dashed in black, and the depth range used to minimize misfit is highlighted in red on the grou Vs profile.

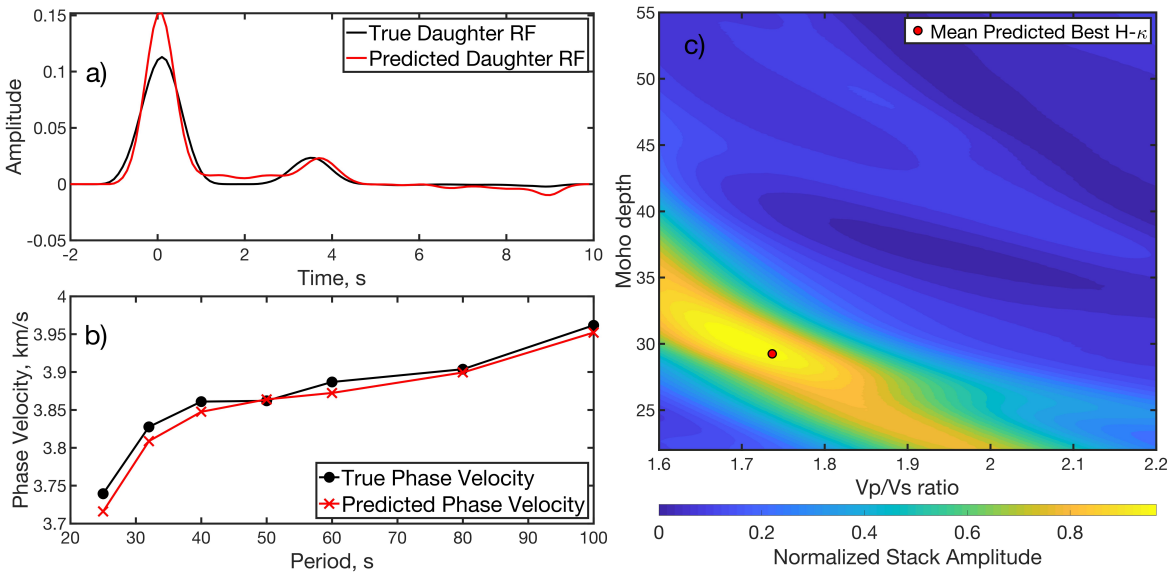

Figure S8. ds08. a) The predicted and observed receiver function data for station ABMD. The observed receiver function is shown in black, the mean of the ensemble of well-fit models is shown in red. b) The observed surface waves (black) and predicted (red) surface waves. c) The H-κ surface after normalization. Warmer colors indicate higher amplitudes. The H-κ result of the mean model is plotted in red.

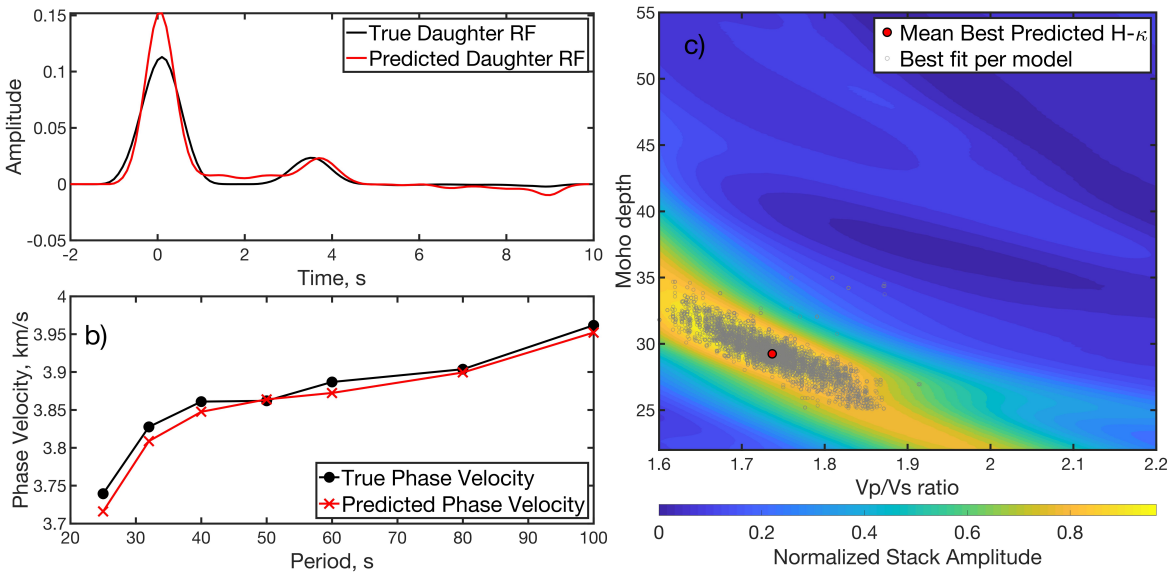

Figure S9. ds09. The same figure as above, but c) now contains the H-κ of all fit models developed during inversion. Light grey circles denote a single model.

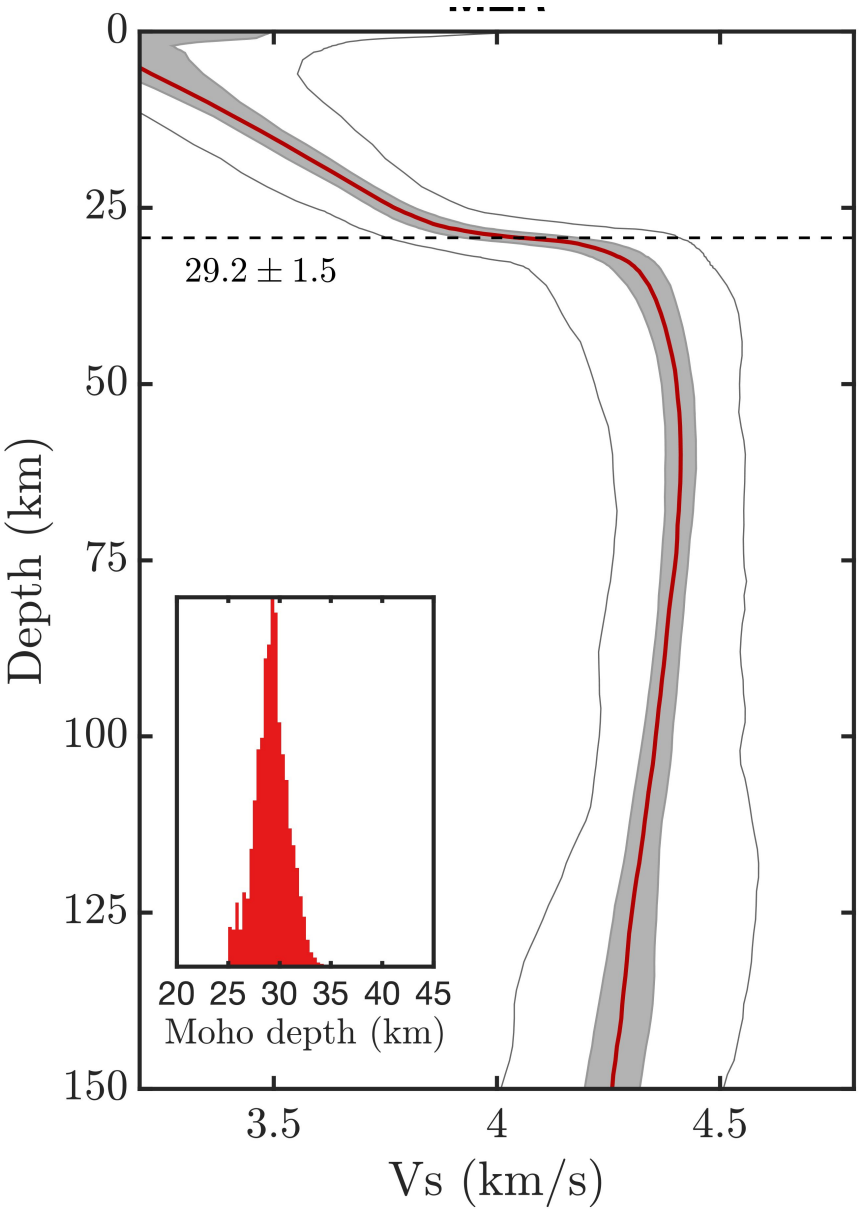

Figure S10. ds10. The shear velocity model of station ABMD. The mean velocity model is plotted in red, the 1σ patched in grey, and the 2σ patched in white bounded by light grey. The histogram of Moho depths is shown in the bottom left. The maximum of the Moho distribution and distribution standard deviation are labelled and displayed as a dashed horizontal black line.

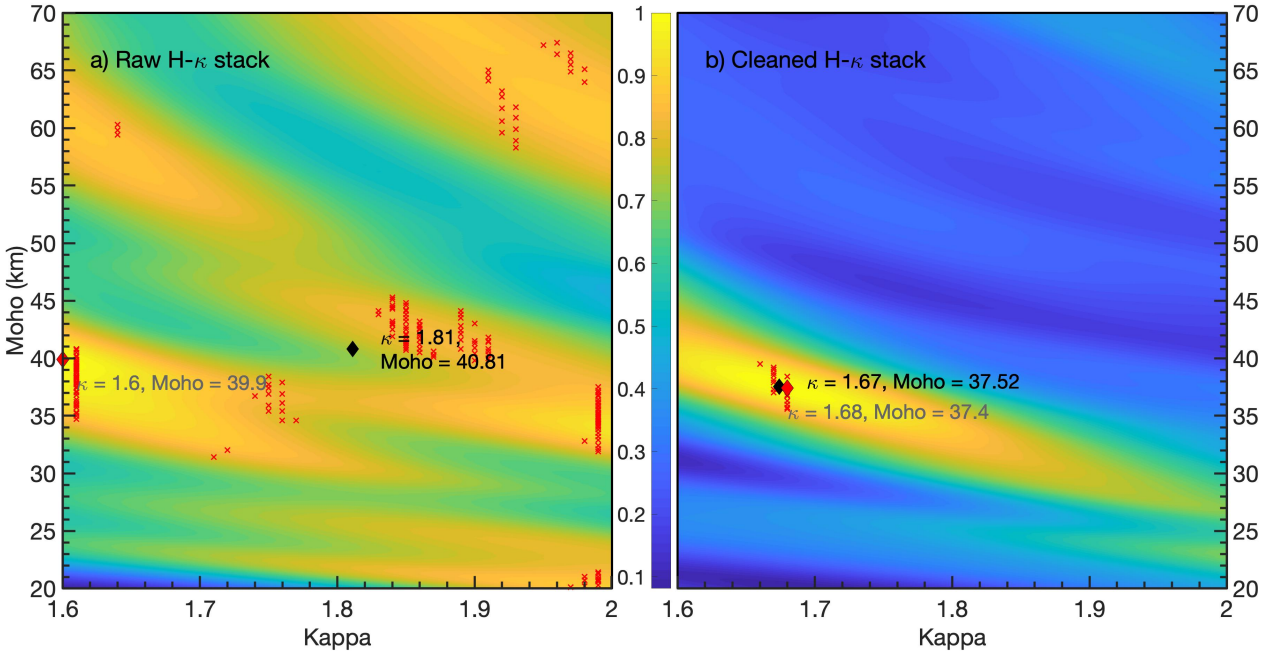

Figure S11. ds11. The results of the cleaned vs raw H-κ stacking procedure. a) shows the results of 5000 H-κ model iterations with randomly perturbed parameters. The red crosses are the best fit H-κ value for a single model iteration. The black diamond is the mean of those models, with corresponding κ and Moho values labelled in black. The red diamond (at the left edge of the surface) is the maximum of the error surface, with the corresponding κ and Moho values labelled in grey. b) shows the results of 5000 H-κ model iterations with randomly perturbed parameters after the DBSCAN process. The black diamond is the mean of those models, with the corresponding κ and Moho values labelled in black. The red diamond is the maximum of the error surface, with the corresponding κ and Moho values labelled in grey. The summed H-κ surfaces are shown in the background for both the raw and cleaned stacks, color coded by the same normalized amplitude scale.